CrystEngComm

ROYAL SOCIETY OF CHEMISTRY

PAPER

View Article Online
View Journal

Cite this: DOI: 10.1039/d5ce00630a

Influence of varying the nickel salt aqueous subphase on the formation of Ni_3(hexaiminotriphenylene)$_2$ metal–organic framework nanosheets at the air/liquid interface†

Kazuaki Tachimoto,[a] Kanokwan Jumtee Takeno[b] and Rie Makiura *[b]

Metal–organic framework (MOF) nanosheets synthesized at the air/liquid interface exhibit properties, such as electrical conductivity, that are highly dependent on their structural attributes, including morphology, lateral dimensions, thickness, crystallinity, and orientation. Achieving precise control over these features, however, remains a significant challenge. Extending our previous works on the air/liquid interfacial synthesis of uniaxially oriented Ni_3(HITP)$_2$ nanosheets (**HITP-Ni-NS**), this study explores the profound influence of the metal salt counterion—a key parameter in MOF crystallization. We present a systematic investigation into how nickel acetate (Ni(OAc)$_2$), nickel chloride ($NiCl_2$), and nickel nitrate (Ni(NO$_3$)$_2$) precursors affect the resulting nanosheet morphology, thickness, crystallinity, and orientation. Our comparative interfacial syntheses demonstrate that variations in the counterion significantly impact crystal growth kinetics, leading to discernible differences in nanosheet architecture. Notably, while $NiCl_2$ and Ni(NO$_3$)$_2$ precursors result in the incorporation of unreacted HATP ligand stacks and subsequent nanosheet disorder, Ni(OAc)$_2$ consistently produces **HITP-Ni-NS** with the greatest thickness and maintains perfect alignment with a preferred ordered crystalline stacking orientation. These observed differences are attributed to variations in the **HITP-Ni-NS** crystal growth mechanism, likely mediated by the distinct pH of the nickel aqueous subphases. These findings highlight the critical role of the metal salt counterion in directing the growth and ultimately tailoring the functional properties of MOF nanosheets.

Received 20th June 2025,
Accepted 24th July 2025

DOI: 10.1039/d5ce00630a

rsc.li/crystengcomm

1. Introduction

Metal–organic frameworks (MOFs) represent a class of crystalline porous materials constructed through the coordination of metal ions and organic ligands.[1–5] Their inherent nanoporosity, characterized by uniform pore dimensions and high structural tunability arising from the vast diversity of their constituent components, has positioned MOFs as promising candidates for a wide range of applications, including selective adsorption,[6–9] gas storage,[10,11] separation,[12–14] and catalysis.[9,15] Furthermore, the compositional flexibility of MOFs enables the design of electrically conductive frameworks, expanding their potential in electronic devices.[16–19] To fully realize the nanotechnological potential of MOFs, particularly in applications such as sensors, transistors, and capacitors, the controlled assembly of their ultrathin films, with precise control over growth direction and thickness, and their integration with other device components are crucial.[20] Achieving precise control over the morphology of MOF thin films, including their lateral dimensions and thickness, is paramount for optimizing their performance in various applications.[21,22]

The air/liquid interface has emerged as a versatile platform for the fabrication of two-dimensional nanomaterials—known as nanosheets—possessing a thickness below 100 nm and high aspect ratio.[23–27] Advances in air/liquid interfacial synthesis have broadened the scope of materials amenable to this technique beyond conventional surfactants, enabling the creation of diverse functional nanosheets, including metal oxides[28,29] and organic[30–32] and organic–inorganic hybrid materials.[20,27,33,34] Similar to a conventional solvothermal synthesis of MOFs, which is governed by a complex interplay of various factors[35,36] such as compositional parameters (component structures, reagent concentrations, type of metal salts, solvent, and pH) and process parameters (temperature and time), the air/liquid

[a] Department of Materials Science, Graduate School of Engineering, Osaka Prefecture University, 1-2 Gakuen-cho, Nakaku, Sakai, Osaka 599-8570, Japan
[b] Department of Materials Science, Graduate School of Engineering, Osaka Metropolitan University, 1-2 Gakuen-cho, Nakaku, Sakai, Osaka 599-8570, Japan. E-mail: rie.makiura@omu.ac.jp

† Electronic supplementary information (ESI) available. See DOI: https://doi.org/10.1039/d5ce00630a

interfacial synthesis of MOFs is also influenced with various factors. Generally, variations in compositional or process parameters, such as surface compression,[37,38] subphase composition and pH,[39–42] concentration of organic ligands,[43] and solvent types,[44] can significantly influence the resulting framework structure and morphology and, consequently, its properties. Therefore, understanding how variations in synthesis conditions at the air/liquid interface can be utilized to tune the morphology of MOF nanosheets represents a critical area of research for advancing their integration into next-generation nanotechnologies.

The fabrication of two dimensional (2D) conductive MOF nanosheets with electrical conductivities exceeding 10^{-4} S cm^{-1} through air/liquid interfacial synthesis has been reported.[21,45–49] Among these materials, $Ni_3(HITP)_2$ (HITP = 2,3,6,7,10,11-hexaiminotriphenylene), a 2D conductive MOF assembled from triphenylene-derived ligands, has gathered significant attention.[50,51] This MOF, characterized by its hexagonal nanoporous architecture, exhibits notable electrical conductivity in its bulk pellet,[50] thin film,[50] and microcrystalline forms.[51] The conduction mechanisms in $Ni_3(HITP)_2$ vary between the inter- and intralayer directions,[51] and the material's bulk electrical properties are substantially modified by the angles and distances of its crystal boundaries.[52] The ability to produce $Ni_3(HITP)_2$ nanosheets with well-controlled crystal alignment could significantly advance ongoing research efforts. Our group has previously achieved the successful fabrication of uniaxially oriented nanosheets of $Ni_3(HITP)_2$ (**HITP-Ni-NS**) with high electrical conductivity from the reaction between 2,3,6,7,10,11-hexaaminotriphenylene (HATP) and Ni^{2+} ions *via* the air/liquid interfacial synthesis.[21] Furthermore, we have already elucidated the impact of solvent selection,[44] the period of standing time for reaction,[53] and how the concentrations of the ligand, HATP,[43] affect the characteristics of the resulting nanosheets. This study now turns its attention to another aspect of MOF nanosheet synthesis: the influence of the metal salt and its counterion—a recognized critical factor in both crystallization and crystal growth processes of MOFs.[54–57] Herein, we present an investigation into the effects of counterions of the nickel salt precursor on the morphology, thickness, crystallinity, and orientation of resulting nanosheets (hereafter denoted as **HATP_Ni**) synthesized with HATP on the air/liquid interface employing three distinct nickel salt species: $Ni(OAc)_2{\cdot}4H_2O$, $NiCl_2{\cdot}6H_2O$, and $Ni(NO_3)_2{\cdot}6H_2O$.

2. Experimental

2.1. Materials

2,3,6,7,10,11-Hexaaminotriphenylene·6HCl (HATP·6HCl) was synthesized according to the literature.[53] Nickel(II) acetate tetrahydrate ($Ni(OAc)_2{\cdot}4H_2O$, ≥99%) was obtained from Kanto Chemical or FUJIFILM Wako Pure Chemical Corporation. Nickel(II) chloride hexahydrate ($NiCl_2{\cdot}6H_2O$, ≥99%), nickel(II) nitrate hexahydrate ($Ni(NO_3)_2{\cdot}6H_2O$, ≥99%), and methanol (MeOH, ≥99%) were obtained from Kanto Chemical. All chemicals and solvents were used without further purification.

2.2. Preparation of the HATP spread solution

The ligand, HATP·6HCl (abbreviated hereafter as HATP), was dissolved in MeOH at room temperature (20–22 °C) to prepare a spread solution with a concentration of 0.59 mM. To ensure complete dissolution, the solution underwent three iterative cycles, each consisting of a 10 second sonication in a water bath followed by magnetic stirring at 600–700 rpm for 5 min. To mitigate potential degradation, the HATP solution was stored under a nitrogen atmosphere in the dark at 4 °C and used within the day of preparation. Furthermore, the integrity of the solution, with specific attention to degradation products and impurities, was assessed *via* ultraviolet-visible–near infrared (UV-vis–near IR) spectroscopy prior to each use.

2.3. Synthesis of HATP_Ni at the air/liquid interface

Aqueous subphase solutions of $Ni(OAc)_2{\cdot}4H_2O$, $NiCl_2{\cdot}6H_2O$, or $Ni(NO_3)_2{\cdot}6H_2O$ were prepared in ultrapure water at a concentration of 50 mM. These solutions were sonicated for 60 min at 20–22 °C to facilitate complete dissolution and were utilized on the day of preparation. A polytetrafluoroethylene (PTFE)-coated Langmuir trough (KSV-NIMA Co. Ltd., $L \times W \times H$ = 364 × 75 × 7 mm^3, surface area between barriers: 318 × 75 mm^2) was filled with the subphase solution to form a meniscus above its top edge. Subsequently, the subphase surface underwent aspiration for cleaning, resulting in a final volume of approximately 220 mL. The temperature of the subphase solution in the Langmuir trough was controlled at 20–21 °C using a water-cooling circulator.

The HATP spread solution (0.59 mM) was carefully spread onto the aqueous subphase surface in the Langmuir trough over a period of 8 to 12 minutes. The spread volumes were 800 μL for the $Ni(NO_3)_2{\cdot}6H_2O$ subphase and 890 μL for the $Ni(OAc)_2{\cdot}4H_2O$ and $NiCl_2{\cdot}6H_2O$ subphases. Subsequently, the subphase temperature was stabilized at 20–21 °C for 60 min. Following equilibration, the surface film was compressed symmetrically from both ends of the trough using PTFE barriers at a compression rate of 10 mm min^{-1}. Surface pressure (π)–mean molecular area (A) isotherms were then recorded using a Wilhelmy plate.

2.4. Deposition of HATP_Ni on solid substrates

HATP_Ni at the air/liquid interface were deposited onto solid substrates (silicon wafers or quartz glass) by horizontally contacting the substrate surface to the interface at room temperature in air (Langmuir–Schaefer technique). For different measurements, specific constant surface pressure was maintained during the transfer process: 5 mN m^{-1} for AFM, 10 mN m^{-1} for UV-vis–near IR, and 20 mN m^{-1} for FTIR and XRD. These surface pressures were precisely controlled

through the symmetric compression of the Teflon barriers from both ends of the trough at a speed of 3.0 mm min^{-1}. Prior to deposition, silicon and quartz substrates were ultrasonically cleaned in MeOH for 30–60 min. **HATP_Ni** readily adhere to cleaned solid substrates, a phenomenon largely driven by diverse non-covalent interactions, including van der Waals forces, hydrogen bonding, and/or Coulombic interactions.[58] Following the transfer of **HATP_Ni** onto the substrate, the samples were immersed in ultrapure water for 10 seconds to remove any unreacted Ni^{2+} ions. Subsequently, the substrates were dried under a stream of N_2 gas or compressed air. The deposited films were then protected from light and stored under argon atmosphere.

2.5. Preparation of HATP nanosheets at the air/pure-water interface and deposition on solid substrates

HATP nanosheets were prepared at the surface of the ultrapure water subphase in the absence of Ni^{2+} ions (hereafter denoted as **HATP_water**). The preparation process and conditions mirrored those of **HATP_Ni**, with the sole exception that ultrapure water was used as the subphase. The conditions for depositing the nanosheets onto substrates were also identical to those described for **HATP_Ni**.

2.6. Brewster angle microscopy at the air/liquid interface

The morphology and surface coverage of **HATP_Ni** and **HATP_water** at the air/liquid interface were investigated using Brewster angle microscopy, BAM (KSV-NIMA, MicroBAM system), under ambient atmospheric conditions. A laser with a wavelength of 659 nm was directed at the air/liquid interface with an incident angle of 53°. BAM images, with dimension of 3 × 4 mm^2, were acquired by detecting the reflected laser light using a charge-coupled device (CCD) camera.

2.7. Ultraviolet-visible-near infrared absorption spectroscopy

Ultraviolet-visible–near infrared (UV-vis-near IR) absorption spectra were acquired in the wavelength range of 190–2700 nm at room temperature under atmospheric conditions using a JASCO V-670 spectrophotometer. All measurements for HATP solutions, as well as **HATP_Ni** and **HATP_water** deposited on quartz substrates were performed using the transmission mode.

2.8. Fourier transform infrared (FTIR) absorption spectroscopy

Fourier transform infrared (FTIR) spectra of **HATP_Ni** deposited on high-resistivity Si substrates were recorded using a JASCO FT-IR-6200 spectrometer within the range of 4000–400 cm^{-1} under vacuum at room temperature. Additionally, FTIR spectra of powder samples of HATP, $Ni(OAc)_2{\cdot}4H_2O$, and $Ni(NO_3)_2{\cdot}6H_2O$ prepared by the KBr pellet technique were obtained under identical measurement conditions.

2.9. Atomic force microscopy

Atomic force microscopy (AFM) was employed using an SPA400 (SII) to obtain surface images of **HATP_Ni** and **HATP_water** deposited on low-resistivity Si substrates. Sample imaging was performed in the dynamic force mode at room temperature in air. All images were acquired using a Si microcantilever with Al back coating (Si-DF20). For each sample, a minimum of four AFM images were obtained and subjected to statistical analysis to determine the nanosheet thickness.

2.10. X-ray crystallography

Grazing incidence (GI) synchrotron X-ray diffraction (XRD) and out-of-plane (θ–2θ geometry) XRD measurements were conducted on **HATP_Ni** deposited on Si substrates with a multiaxis diffractometer at the BL19B2 beamline in SPring-8. XRD measurements were also performed using a SmartLab (Rigaku) with a Cu K_α source operating at a wavelength (λ) of 1.5418 Å. Both GI in-plane and θ–2θ geometric XRD scans were conducted. For both configurations, the glancing angle (ω) was optimized to maximize the peak intensity corresponding to the 100 reflection (GI-XRD) or to the 001 reflection (out-of-plane XRD). A Soller collimator (0.114°) was positioned in front of a D/tex detector. A nanosheet deposited on a high-resistivity Si substrate was used for these measurements.

3. Results and discussion

3.1. Formation of HATP_Ni at the air/liquid interface

The synthesis of **HATP_Ni** at the air/liquid interface involves the reaction of HATP ligands with Ni^{2+} ions present in an aqueous subphase (Fig. 1). The **HATP_Ni** comprises planar honeycomb networks of **HITP-Ni-NS**, with layers stacked *via* π–π interactions.[21,52] To investigate the influence of nickel salts, three aqueous subphase solutions containing different Ni^{2+} sources were prepared: $Ni(OAc)_2{\cdot}4H_2O$, $NiCl_2{\cdot}6H_2O$, or $Ni(NO_3)_2{\cdot}6H_2O$. A methanol solution of HATP ligands was then carefully spread onto each subphase with the spreading rate controlled. Upon completion of the HATP solution spreading onto the aqueous subphase, the interface was

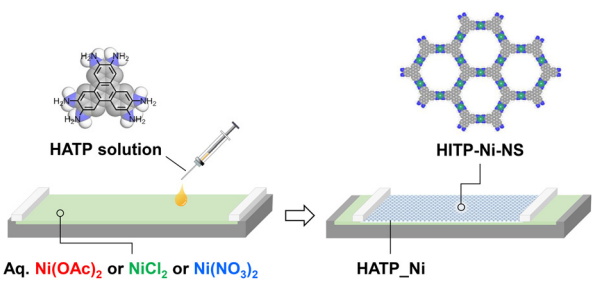

Fig. 1 Schematic illustration of the synthetic procedure for **HATP_Ni** at the air/liquid interface, utilizing various nickel salt precursors. **HATP_Ni** is characterized by planar honeycomb networks of **HITP-Ni-NS**, with π–π interactions facilitating the stacking of each layer.

maintained undisturbed for 60 min. Subsequently, the synthesized **HATP_Ni** on the subphase surface was gathered by controlled compression using PTFE barriers and deposited onto solid substrates for further analysis. **HATP_Ni** fabricated for each Ni^{2+} containing subphase was labelled as **HATP_Ni(OAc)$_2$**, **HATP_NiCl$_2$**, and **HATP_Ni(NO$_3$)$_2$**. For comparative purposes, the HATP solution was also spread onto a surface of the ultrapure water subphase, followed by the collection and deposition of the resulting **HATP_water** onto solid substrates.

The formation of **HATP_Ni** at the air/liquid interface was monitored with surface pressure (π) – mean molecular area (A) isotherms (Fig. 2, left panel). Representative π–A isotherms for **HATP_Ni** synthesized on subphases of $Ni(OAc)_2$, $NiCl_2$, and $Ni(NO_3)_2$, alongside that of **HATP_water**, are presented in Fig. 2a, d, g, and j, respectively. Mechanical compression of the surface with two barriers resulted in a monotonic increase in π, indicating the occurrence of the nanosheet formation process. Notably, the initial onset of the steep π increase (A values) was consistent across all samples. The first inflection point was assigned to the sharp transition at ~0–3 mN m^{-1}. To accurately determine the second inflection points, which presented a gradual transition, a first-derivative analysis of the π–A isotherm was performed. This analysis was subsequently refined by visual inspection to pinpoint abrupt changes in the slope of the isotherms and their first derivative. While the first inflection points (~0–3 mN m^{-1}) and slopes of the isotherms exhibited no significant variation, the second inflection points in the π–A isotherms displayed considerable difference ranging from 31 to 51 mN m^{-1}. Specifically, the surface pressure at the second inflection point was lowest for **HATP_water** (π = 36 ± 2 mN m^{-1}), followed by **HATP_Ni(OAc)$_2$** (π = 38.3 ± 0.9 mN m^{-1}). In contrast, significantly higher values were observed for **HATP_NiCl$_2$** (π = 48.8 ± 1.5 mN m^{-1}), and **HATP_Ni(NO$_3$)$_2$** (π = 50.4 ± 1.3 mN m^{-1}). We noted that the slightly increased uncertainty associated with the second inflection points of **HATP_water**, relative to other samples, primarily stemmed from the fluctuating nature of **HATP** domains during film compression. We hypothesize that the elevated surface pressure for **HATP_NiCl$_2$** and **HATP_Ni(NO$_3$)$_2$** indicates increased mechanical strength of their respective nanosheet thin films under surface compression, potentially attributable to heterogeneous compositions within these films. The interfaces between these different domains, as well as the interactions within and between the different components, probably contribute significantly to the film's resistance to compression. The observed variation in the second inflection points suggests a correlation with the distinct roles of the counterions of nickel precursors in the formation of the **HATP_Ni** structure under compression.

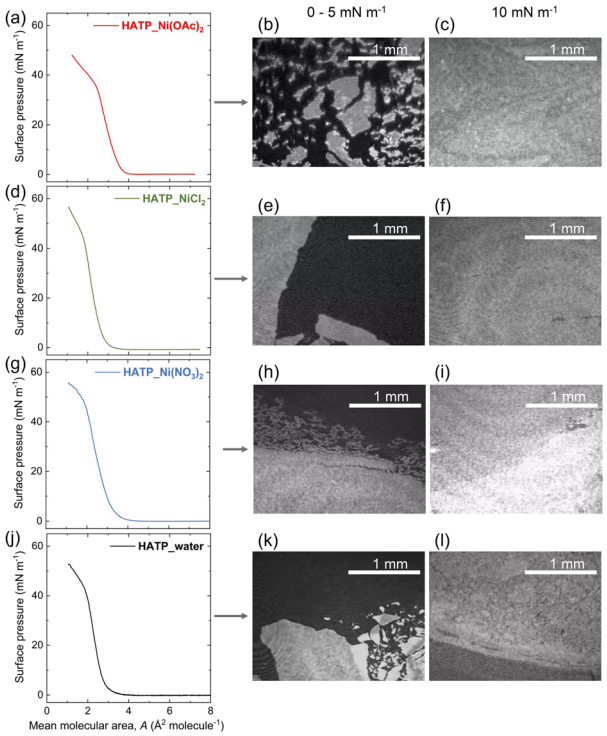

Fig. 2 *In situ* observation of the formation, morphology, and surface coverage of **HATP_Ni** at the air/liquid interface with π–A isotherms and Brewster angle microscopy (BAM). The representative π–A isotherms of (a) **HATP_Ni(OAc)$_2$** (red), (d) **HATP_NiCl$_2$** (green), (g) **HATP_Ni(NO$_3$)$_2$** (blue), and (j) **HATP_water** (black). BAM images of the corresponding π–A isotherms at π = 0–5 mN m^{-1} and 10 mN m^{-1} on the millimetre scale: (b and c) **HATP_Ni(OAc)$_2$**, (e and f) **HATP_NiCl$_2$**, (h and i) **HATP_Ni(NO$_3$)$_2$**, and (k and l) **HATP_water** as a reference material. A scale bar is 1 mm.

Complementary *in situ* BAM analysis (Fig. 2, right panel) provided real-time insights into the morphology and surface coverage of **HATP_Ni** at the air/liquid interface. Prior to the sharp increase in surface pressure (π < 5 mN m^{-1}), BAM images of all **HATP_Ni** samples (Fig. 2b, e and h) and **HATP_water** (Fig. 2k) revealed a morphology characterized by the coexistence of small and large island-like assemblies separated by significant inter-assembly gaps. Upon compression to a higher surface pressure (π = 10 mN m^{-1}), BAM images indicated increased contact and reduced inter-assembly gaps for all **HATP_Ni** samples (Fig. 2c, f and i) and **HATP_water** (Fig. 2l). Notably, under compression, all observed **HATP_Ni** samples displayed relatively uniform thin film morphologies of without prominent features, suggesting homogeneity at the macroscopic scale. While the macroscopic morphology and surface coverage observed *via* BAM and the overall shape of the π–A isotherms did not exhibit significant differences among the **HATP_Ni** synthesized with various nickel salt precursors, notable variations were observed in the surface pressure at the second inflection during film compression. Specifically, **HATP_NiCl$_2$** and **HATP_Ni(NO$_3$)$_2$** displayed significantly higher surface pressures at this point. This implies that the kinetics of **HITP-Ni-NS** crystal growth and/or assembly processes are significantly influenced by the selection of nickel salt precursors. We hypothesize that the elevated mechanical strength observed in **HATP_NiCl$_2$** and **HATP_Ni(NO$_3$)$_2$** under surface compression stems from the

potential presence of unreacted HATP ligands within the synthetic systems. These unreacted ligands may facilitate the formation of vertically aligned HATP molecules through π–π stacking. The subsequent incorporation of these unreacted HATP domains between the **HITP-Ni-NS** assemblies could enhance the film's resistance to compression. This proposed structural characteristic appears to be less prevalent in **HATP_Ni(OAc)$_2$**, where a more complete reaction between HATP ligands and Ni^{2+} is inferred, potentially leading to a more homogeneous film structure.

3.2. *Ex situ* surface observation of HATP_Ni

Atomic force microscopy (AFM) was employed to further investigate the nanoscale surface coverage and morphology of **HATP_Ni** synthesized with various nickel salt precursors. Specifically, **HATP_Ni** and **HATP_water** deposited on Si substrates at π = 5 mN m^{-1} were analysed. Topographical AFM images, representative thickness profiles selected from the images along the red line, and thickness histograms are shown in Fig. 3. The topographical images of **HATP_Ni** synthesized with Ni^{2+} reveal the hierarchical assembly of primary **HITP-Ni-NS** crystals (Fig. 3a, d and g), characterized by round-shaped nanosheets with lateral dimensions of the order of tens of nanometers, into larger secondary assemblages. In contrast, **HATP_water**, lacking these primary **HITP-Ni-NS** crystals, exhibits only a homogeneous distribution of nanosheets (Fig. 3j). Notably, **HATP_Ni(OAc)$_2$** exhibits the highest concentration of these primary **HITP-Ni-NS** crystals. Subsequent thickness analysis was performed on the AFM images of each sample, and representative thickness profiles are presented in Fig. 3b, e, h and k. The thickness distribution for **HATP_Ni** synthesized with various nickel salt precursors was further quantified through histograms, and the average thickness values were compared (Fig. 3c, f, i and l). The average thicknesses of **HATP_Ni(OAc)$_2$**, **HATP_NiCl$_2$**, and **HATP_Ni(NO$_3$)$_2$**, as well as **HATP_water**, were determined to be 4.6(2), 2.78(7), 2.46(7), and 2.30(5) nm, respectively. Detailed examination of the thickness distribution revealed that **HATP_NiCl$_2$** and **HATP_Ni(NO$_3$)$_2$** exhibited narrow distributions, displaying a similar trend to that observed for **HATP_water**. Conversely, **HATP_Ni(OAc)$_2$** showed a broader thickness distribution and the largest average nanosheet thickness. We hypothesize that the reaction rate of crystal growth of **HITP-Ni-NS** for **HATP_Ni(OAc)$_2$** is faster than those of **HATP_NiCl$_2$** and **HATP_Ni(NO$_3$)$_2$**. These findings indicate that the choice of the nickel salt precursor possibly impacts the crystal growth kinetics of **HITP-Ni-NS**, thereby governing the thickness and uniformity of the synthesized **HATP_Ni**.

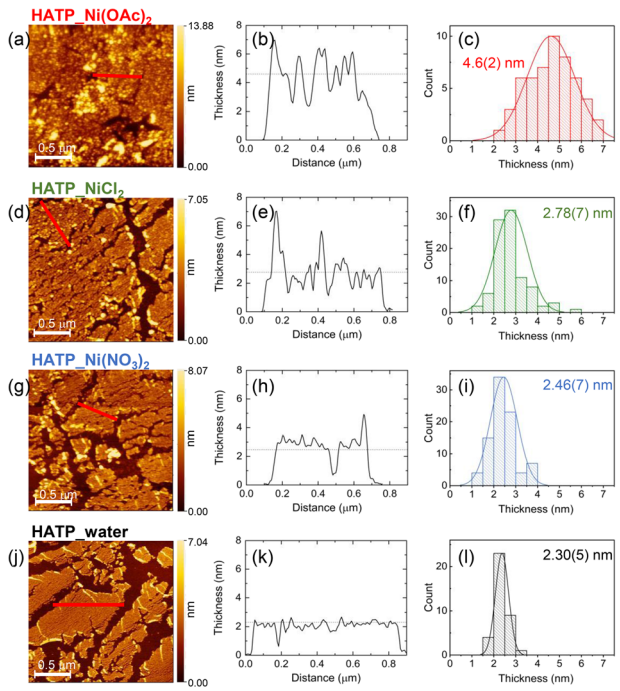

Fig. 3 *Ex situ* atomic force microscopy (AFM) for surface observation of the nanoscale surface coverage and morphology of thin films deposited on Si substrates at π = 5 mN m^{-1}. (a), (d), and (g) show **HATP_Ni** synthesized using Ni(OAc)$_2$,[43] NiCl$_2$, and Ni(NO$_3$)$_2$ precursors, respectively, and (j) displays **HATP_water** prepared under identical deposition conditions. (b), (e), (h), and (k) display representative thickness profiles measured along the red lines depicted in the corresponding AFM topographical images. Vertical dotted lines indicate the average thickness, calculated from at least four nanosheet images. (c), (f), (i), and (l) display the corresponding thickness histograms and average thickness values for **HATP_Ni(OAc)$_2$**, **HATP_NiCl$_2$**, **HATP_Ni(NO$_3$)$_2$**, and **HATP_water**, respectively.

3.3. Electronic states and coordination bonds of HITP-Ni-NS

UV-vis-near-IR spectroscopy was employed to analyse **HATP_Ni** samples prepared with different nickel precursors. The resulting spectra (Fig. 4a and b) show characteristic absorption bands at ~624 nm, attributed to d–d* transitions

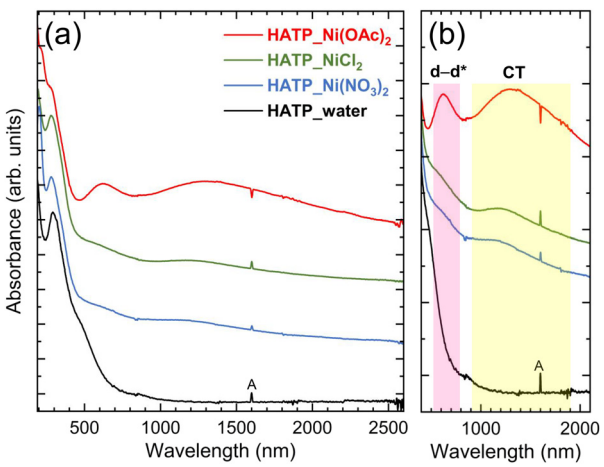

Fig. 4 Ultraviolet (UV)-visible (vis)-near infrared (IR) spectra of nanosheets deposited on quartz substrates. (a) Spectra of **HATP_Ni** synthesized using various nickel salt precursors and **HATP_water**. (b) Enlarged view of absorption bands associated with d–d* transition at 624.5 nm and charge transfer (CT) between HITP and Ni^{2+} at ~1200 nm. Absorbance spectra were normalized at 280 nm. Feature 'A' indicates instrumental artifacts arising from light source switching.

in Ni^{2+}, and at ~1255 nm, corresponding to charge transfer (CT) between Ni^{2+} and HITP. These spectral features indicate the presence of Ni^{2+} ions, an alteration in the ligand field symmetry of their d-orbital upon coordination to HITP ligands, and the establishment of electronic interactions through coordination bonds under all examined synthesis conditions. Notably, the CT transition exhibited its highest intensity in **HATP_Ni(OAc)$_2$** compared to **HATP_NiCl$_2$** and **HATP_Ni(NO$_3$)$_2$**, which implies a greater extent of Ni^{2+}–HITP coordination within the **HITP-Ni-NS** for **HATP_Ni(OAc)$_2$**. For **HATP_Ni(OAc)$_2$**, **HATP_NiCl$_2$**, and **HATP_Ni(NO$_3$)$_2$**, the peak height ratios of the charge transfer (CT) band (~1255 nm) to the unreacted HATP ligand band (288 nm) were calculated to be 0.47, 0.17, and 0.17, respectively. This trend correlates with a higher synthetic yield of **HATP_Ni(OAc)$_2$** relative to the other samples. Fourier transform infrared (FTIR) spectroscopy was also employed to investigate the coordination bonds (Fig. S1†). The FTIR spectra of **HATP_Ni(OAc)$_2$**, **HATP_NiCl$_2$**, and **HATP_Ni(NO$_3$)$_2$** revealed a redshift in the NH stretching peaks (~3500–3250 cm^{-1}, Fig. S1a†) and a dominant CN stretching band (~1330 cm^{-1}) relative to the NH bending band (~1640 cm^{-1}) (Fig. S1b†). These observations provide evidence for the formation of **HITP-Ni-NS** within all investigated **HATP_Ni**. The more pronounced decrease in the NH bending peak observed for **HATP_Ni(OAc)$_2$** compared to **HATP_NiCl$_2$** and **HATP_Ni(NO$_3$)$_2$** suggests a higher degree of N–Ni bond formation in **HATP_Ni(OAc)$_2$**. Analyses by both UV-vis-near IR and FTIR spectroscopy confirm the successful formation of **HITP-Ni-NS** in all **HATP_Ni** samples under investigation. Notably, the synthetic yield of **HITP-Ni-NS** was greatest when $Ni(OAc)_2$ served as a nickel salt precursor.

The formation of the HITP and Ni^{2+} complex at the air/liquid interface is facilitated by the deprotonation of HATP into HITP.[21] A relatively alkaline reaction environment is conductive to the acid–base equilibrium of HATP shifting towards its deprotonated HITP form, which consequently enhances coordination between HITP and Ni^{2+} for the formation of **HITP-Ni-NS**.[59] The pH values of the aqueous subphase were measured to be 7.4, 5.6, and 4.8 for syntheses employing $Ni(OAc)_2$, $NiCl_2$, and $Ni(NO_3)_2$, respectively. In the absence of pH control agents, the formation of **HATP_Ni** was demonstrably influenced by the inherent pH of the subphase, which varied significantly depending on the nickel salt precursor utilized. Moreover, the unique counterions present in each nickel salt exert an influence on the hydrolysis equilibria of the metal ions within the subphase. Notably species such as Cl^- and NO_3^- possess the capacity to compete with HITP for coordination sites on the metal ions,[60] thereby altering the local concentration of reactive Ni^{2+} species. The competition reaction could not be definitively confirmed in our current investigations, as Ni^{2+} and its associated counterions were fully removed during the nanosheet purification steps (Fig. S1a†). Nevertheless, its occurrence is considered highly plausible. Consequently, **HATP_NiCl$_2$** and **HATP_Ni(NO$_3$)$_2$**, which formed under relatively acidic conditions, exhibited lower concentrations of deprotonated HITP, leading to slower crystal growth rates of **HITP-Ni-NS**[36] and substantial incorporation of unreacted HATP domains. The enhanced uniformity in nanosheet thickness observed with AFM (Fig. 3e and h) for in **HATP_NiCl$_2$** and **HATP_Ni(NO$_3$)$_2$** compared to **HATP_Ni(OAc)$_2$** (Fig. 3b) is likely attributable to a higher incorporation of unreacted HATP domains during their syntheses. Conversely, the nucleation rate of **HITP-Ni-NS** in the **HATP_Ni(OAc)$_2$** was accelerated, yielding a considerable number of nanocrystals that occasionally promoted stacking through various mechanisms.

3.4. Crystalline structure and orientation

The influence of nickel salt precursors on the crystallinity and orientation of **HITP-Ni-NS** in the synthesized **HATP_Ni** was investigated by GI in-plane XRD measurements. Fig. 5 displayed GI in-plane XRD profiles for **HATP_Ni(OAc)$_2$**, **HATP_NiCl$_2$**, and **HATP_Ni(NO$_3$)$_2$**. The GI in-plane XRD profile of **HATP_Ni(OAc)$_2$** revealed Bragg reflections exclusively indexed to the *hk*0 planes of a metrically hexagonal lattice, thereby confirming the uniaxial orientation of the **HITP-Ni-NS**.[21,43] Conversely, the XRD profiles obtained from **HATP_NiCl$_2$** and **HATP_Ni(NO$_3$)$_2$** exhibited significantly attenuated *hk*0 reflection peaks, alongside a more pronounced Bragg reflection indexed as 001. This spectral difference implies a comparatively lower degree of structural orientation in these samples relative to **HATP_Ni(OAc)$_2$**.

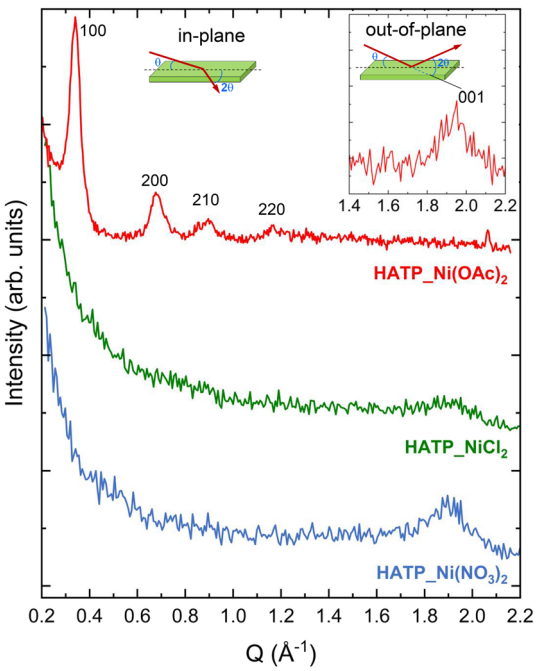

Fig. 5 Structural and orientational characterization of **HATP_Ni** deposited on Si substrates. GI in-plane XRD profiles for **HATP_Ni(OAc)$_2$** (red), **HATP_NiCl$_2$** (green), and **HATP_Ni(NO$_3$)$_2$** (blue). The inset profile shows the out-of-plane XRD profile for **HATP_Ni(OAc)$_2$** of the 001 peak at ≅1.9 Å.

Furthermore, an increased ratio of the *hk*0 reflection peak intensity to the 001 peak indicates that the lateral domain sizes of the **HITP-Ni-NS** crystals are substantially larger in **HATP_Ni(OAc)$_2$** than in **HATP_NiCl$_2$** and **HATP_Ni(NO$_3$)$_2$**. The orientation of **HATP_Ni** was further investigated through out-of-plane XRD analysis. A consistent single peak was detected at Q ~1.9 Å^{-1} across all **HATP_Ni** samples, including **HATP_Ni(OAc)$_2$** (Fig. 5 inset, Fig. S2†), **HATP_NiCl$_2$**, and **HATP_Ni(NO$_3$)$_2$** (Fig. S2†). This observation indicates a highly ordered π–π stacked crystal arrangement oriented vertically to the surface.

The proposed **HITP-Ni-NS** crystalline structure, derived from the GI in-plane XRD measurement, consistently manifests a uniaxial orientation, with in-plane lattice parameters of $a = b$ ~21.4 Å (Fig. 6a). This layered motif is further supported by out-of-plane XRD measurement, which attribute to π–π stacking between individual nanosheets, resulting in an interlayer distance of d ~3.2 Å (Fig. 6a), consistent with a previous report.[21] Crystallite size analysis of **HATP_Ni** was subsequently conducted by employing the full width at half maximum (FWHM) of the 001 reflection. The crystallite size derived from the 001 reflection in the out-of-plane XRD profiles provided specific information regarding the stacking arrangement and thickness of the nanosheet layers. Additionally, we aimed to elucidate the molecular stacking of unreacted HATP domains within the nanosheet *via* analysis of the 001 peak of the GI in-plane XRD profiles. However, due to the highly preferential orientation of **HATP_Ni(OAc)$_2$**, which is established during air/liquid interface growth, the 001 reflection (indicative of perpendicular stacking order) is entirely absent in its GI in-plane XRD profile. For these reasons, the crystallite size analysis utilized the GI in-plane profiles for **HATP_NiCl$_2$** and **HATP_Ni(NO$_3$)$_2$** and the out-of-plane profile for **HATP_Ni(OAc)$_2$**. Notably, the FWHM values derived from the GI in-plane profiles for **HATP_NiCl$_2$** and **HATP_Ni(NO$_3$)$_2$** exhibited good agreement with those obtained from their respective out-of-plane XRD profiles. The crystallite sizes for **HATP_Ni(OAc)$_2$**, **HATP_NiCl$_2$**, and **HATP_Ni(NO$_3$)$_2$** were determined to be 3.99(14) nm, 2.6(2) nm, and 2.1(2) nm, respectively. Notably, the largest crystallite size observed for **HATP_Ni(OAc)$_2$** indicates that the synthesis conditions employed for the Ni(OAc)$_2$ precursor were most conducive to crystallite growth. This trend correlates with the increased nanosheet thickness as determined by AFM measurements.

3.5. Proposed crystalline structure and orientation of HATP_Ni synthesized using various nickel salt precursors

The formation of **HATP_Ni(OAc)$_2$** at the air/liquid interface has been proposed *via* a two-stage mechanism:[53] (i) interfacial deprotonation of HATP followed by the spontaneous nucleation and growth of primary **HITP-Ni-NS** nanocrystals through coordination bonding between the deprotonated HITP ligand and Ni^{2+} ions at the interface, and (ii) subsequent lateral assembly of these primary nanocrystals into larger nanosheets, accompanied by the dissolution of unreacted HATP ligands into the aqueous subphase. Notably, the standing time of 60 min, used in this work, was determined to be critical for achieving optimal interfacial nanosheet quality. Under these conditions, any **HITP-Ni-NS** formed within the subphase from dissolved HATP did not float to and adhere to the pre-formed interfacial **HITP-Ni-NS**, thus preventing the formation of undesirable multi-layered or aggregated structures.

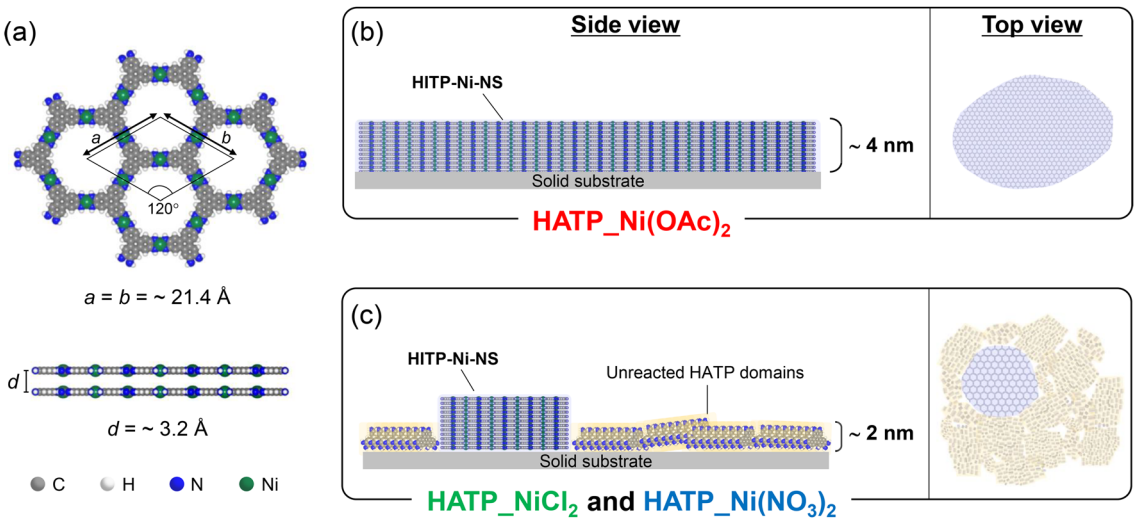

Fig. 6 Proposed crystalline structures of **HATP_Ni** synthesized at the air/liquid interface and deposited on a solid substrate. (a) A simulated crystallite structure illustrating the basal plane projection of **HITP-Ni-NS** and its stacking arrangement.[21] Atomic representations: carbon (grey), hydrogen (white), nitrogen (blue), and Ni^{2+} ions (green). Schematic illustrations (side and top views) depict the morphology of **HATP_Ni** synthesized with different nickel precursors at the air/liquid interface: (b) Ni(OAc)$_2$, and (c) NiCl$_2$ and Ni(NO$_3$)$_2$. Notably, syntheses employing NiCl$_2$ and Ni(NO$_3$)$_2$ resulted in a considerable incorporation of stacking HATP ligands to form unreacted HATP domains.

Alterations in crystal growth kinetics, morphology, thickness, and crystal orientation of **HITP-Ni-NS** were observed to be dependent on the specific nickel salt precursors utilized in the aqueous subphase: $Ni(OAc)_2{\cdot}4H_2O$, $NiCl_2{\cdot}6H_2O$, and $Ni(NO_3)_2{\cdot}6H_2O$. The rates of HATP deprotonation and subsequent **HITP-Ni-NS** nucleation were found to follow the descending order: $Ni(OAc)_2 > NiCl_2 > Ni(NO_3)_2$. These kinetic parameters are demonstrably influenced by both the pH of aqueous subphase and the competitive coordination of Cl^- and NO_3^- with Ni^{2+} ions. The combination of a rapid nucleation rate, an elevated concentration of deprotonated HITP, and a satisfactory local Ni^{2+} concentration collectively promotes the formation of primary nanocrystals and a significant yield of **HITP-Ni-NS** nanocrystals. Moreover, a lower concentration of residual HATP ligands in the $Ni(OAc)_2$ subphase system facilitates the self-assembly of these primary nanocrystals into larger nanosheets with a high degree of crystal orientation. This favourable environment for lateral growth and subsequent increased stacking is observed in **HATP_Ni(OAc)$_2$** (Fig. 6b), resulting in a larger average crystallite size (~4 nm). Based on the interlayer distance of ~3.2 Å, the estimated average number of stacked layers in **HATP_Ni(OAc)$_2$** is approximately 12. Conversely, the slightly acidic pH of the Ni^{2+} subphase when employing $NiCl_2$ and $Ni(NO_3)_2$ does not effectively promote HATP deprotonation, resulting in a slower nucleation rate, a lower degree of lateral growth, and less stacking of **HITP-Ni-NS** for **HATP_NiCl$_2$** and **HATP_Ni(NO$_3$)$_2$**. Consequently, a fraction of the unreacted HATP ligand likely aggregated and became incorporated within the forming **HITP-Ni-NS** crystals at the air/liquid interface, or dissolved into the subphase. The crystallite sizes for **HATP_NiCl$_2$** (~2.6 nm) and **HATP_Ni(NO$_3$)$_2$** (~2.1 nm) as evaluated from the 001 peak in GI in-plane XRD is potentially influenced by the incorporation of unreacted HATP domains. The stacked residual unreacted HATP molecules on the substrate surface are similar in orientation (predominantly vertical or tilted) to those found in **HATP_water**. Considering the approximated 2 nm molecular size of HATP, the higher crystallite size measured for **HATP_NiCl$_2$** and **HATP_Ni(NO$_3$)$_2$** than this value suggests the co-existence of larger **HITP-Ni-NS** crystallites with the stacked residual unreacted HATP domains.

4. Conclusions

Our investigation elucidated the influence of various nickel salt precursors on the morphology, surface coverage, thickness, crystallinity, and orientation of **HATP_Ni** nanostructures synthesized at the air/liquid interface. Through comparative analyses employing $Ni(OAc)_2{\cdot}4H_2O$, $NiCl_2{\cdot}6H_2O$, and $Ni(NO_3)_2{\cdot}6H_2O$ in the aqueous subphase, we demonstrated that counterions significantly modulate **HITP-Ni-NS** crystal kinetics. This modulation gives rise to marked variations in the morphology, thickness, and crystal orientation of the resulting **HATP_Ni** nanostructures. We theorize that these differences stem from distinct crystal growth mechanisms for **HITP-Ni-NS**, which are influenced, at least in part, by variations in the aqueous subphase's pH, the deprotonation rate of HATP, and the local concentration of reactive Ni^{2+} ions. These precursor-dependent factors consequently exert a critical influence on the nucleation and growth kinetics, as well as the preferred self-assembly orientation of **HITP-Ni-NS** at the air/liquid interface. The absence of incorporated domains of unreacted HATP ligands during interfacial synthesis is attributed to the enhancement of structural order. The use of $Ni(OAc)_2$ as a nickel salt precursor resulted in **HATP_Ni** nanosheets that exhibit the most highly ordered crystalline stacking structure of **HITP-Ni-NS**. These nanosheets are also free of impurities and achieve the greatest **HITP-Ni-NS** thickness among all precursors investigated.

Data availability

The data supporting this article have been included as part of the ESI.†

Author contributions

Kazuaki Tachimoto: sample synthesis, characterization, data analysis, and investigation. Kanokwan Jumtee Takeno: data analysis, validation, investigation and writing. Rie Makiura: conceptualization, direction, supervision, data analysis, validation, investigation, writing and funding acquisition.

Conflicts of interest

The authors declare no conflict of interest.

Acknowledgements

This work was supported by JSPS KAKENHI Grant Numbers JP19H05715 (Grant-in-Aid for Scientific Research on Innovative Area: Aquatic Functional Materials), JP20H02551, JP23K17865, JP23KK0255, JP24K01301, JP25H01404 (Grant-in-Aid for Transformative Research Areas (B): Multiply Programmed Layers), the Kumagai foundation for science and technology, the Sumitomo Electric Group CSR Foundation and the Izumi science and technology foundation, Japan. The synchrotron X-ray diffraction experiments were performed at the BL19B2 beamline, SPring-8 (2019A1771, 2019B1860, 2019B1857, 2021A1658). The authors are grateful to Ms. Yuka Susami for her experimental support.

References

1 M. Kondo, T. Yoshitomi, H. Matsuzaka, S. Kitagawa and K. Seki, *Angew. Chem., Int. Ed. Engl.*, 1997, **36**, 1725–1727.

2 H. Li, M. Eddaoudi, M. O'Keeffe and O. M. Yaghi, *Nature*, 1999, **402**, 276–279.
3 O. M. Yaghi, M. O'Keeffe, N. W. Ockwig, H. K. Chae, M. Eddaoudi and J. Kim, *Nature*, 2003, **423**, 705–714.
4 S. Kitagawa, R. Kitaura and S. Noro, *Angew. Chem., Int. Ed.*, 2004, **43**, 2334–2375.
5 S. Horike, S. Shimomura and S. Kitagawa, *Nat. Chem.*, 2009, **1**, 695–704.
6 D. Britt, D. Tranchemontagne and O. M. Yaghi, *Proc. Natl. Acad. Sci. U. S. A.*, 2008, **105**, 11623–11627.
7 K. Yang, F. Xue, Q. Sun, R. Yue and D. Lin, *J. Environ. Chem. Eng.*, 2013, **1**, 713–718.
8 K. Vellingiri, J. E. Szulejko, P. Kumar, E. E. Kwon, K.-H. Kim, A. Deep, D. W. Boukhvalov and R. J. C. Brown, *Sci. Rep.*, 2016, **6**, 27813.
9 P. Li, S. Kim, J. Jin, H. C. Do and J. H. Park, *Appl. Catal., B*, 2020, **263**, 118284.
10 J. P. Marco-Lozar, J. Juan-Juan, F. Suárez-García, D. Cazorla-Amorós and A. Linares-Solano, *Int. J. Hydrogen Energy*, 2012, **37**, 2370–2381.
11 M. K. Taylor, T. Runčevski, J. Oktawiec, M. I. Gonzalez, R. L. Siegelman, J. A. Mason, J. Ye, C. M. Brown and J. R. Long, *J. Am. Chem. Soc.*, 2016, **138**, 15019–15026.
12 Y. Peng, Y. Li, Y. Ban, H. Jin, W. Jiao, X. Liu and W. Yang, *Science*, 2014, **346**, 1356–1359.
13 X. Wang, C. Chi, K. Zhang, Y. Qian, K. M. Gupta, Z. Kang, J. Jiang and D. Zhao, *Nat. Commun.*, 2017, **8**, 14460.
14 P. Cheng, Y. Huang, C. Wu, X. Wang, X. Fu, P. Li, Y. Liu and S. Xia, *J. Membr. Sci.*, 2021, **640**, 119812.
15 S. Yuan, L. Zou, H. Li, Y. Chen, J. Qin, Q. Zhang, W. Lu, M. B. Hall and H. Zhou, *Angew. Chem., Int. Ed.*, 2016, **55**, 10776–10780.
16 A. A. Talin, A. Centrone, A. C. Ford, M. E. Foster, V. Stavila, P. Haney, R. A. Kinney, V. Szalai, F. El Gabaly, H. P. Yoon, F. Léonard and M. D. Allendorf, *Science*, 2014, **343**, 66–69.
17 X. Xu, J. Tang, H. Qian, S. Hou, Y. Bando, M. S. A. Hossain, L. Pan and Y. Yamauchi, *ACS Appl. Mater. Interfaces*, 2017, **9**, 38737–38744.
18 L. S. Xie, G. Skorupskii and M. Dincă, *Chem. Rev.*, 2020, **120**, 8536–8580.
19 S. Tao, J. Wang and J. Zhang, *ACS Nano*, 2025, **19**, 9484–9512.
20 R. Makiura, S. Motoyama, Y. Umemura, H. Yamanaka, O. Sakata and H. Kitagawa, *Nat. Mater.*, 2010, **9**, 565–571.
21 T. Ohata, A. Nomoto, T. Watanabe, I. Hirosawa, T. Makita, J. Takeya and R. Makiura, *ACS Appl. Mater. Interfaces*, 2021, **13**, 54570–54578.
22 T. Lee, J. Kim, C. Park, H. Kim, M. Kim, H. Park, I. Kim, J. Ko, K. Pak, S. Q. Choi, I. Kim and S. Park, *Adv. Mater.*, 2022, **34**, 2107696.
23 J. A. Zasadzinski, R. Viswanathan, L. Madsen, J. Garnaes and D. K. Schwartz, *Science*, 1994, **263**, 1726–1733.
24 T. Nakamura, H. Tachibana, M. Yumura, M. Matsumoto, R. Azumi, M. Tanaka and Y. Kawabata, *Langmuir*, 1992, **8**, 4–6.
25 R. Makiura, K. Tsuchiyama and O. Sakata, *CrystEngComm*, 2011, **13**, 5538–5541.
26 O. N. Oliveira, L. Caseli and K. Ariga, *Chem. Rev.*, 2022, **122**, 6459–6513.
27 R. Makiura, *Coord. Chem. Rev.*, 2022, **469**, 214650.
28 F. Wang, J.-H. Seo, G. Luo, M. B. Starr, Z. Li, D. Geng, X. Yin, S. Wang, D. G. Fraser, D. Morgan, Z. Ma and X. Wang, *Nat. Commun.*, 2016, **7**, 10444.
29 Y. Wang, Y. Shi, Z. Zhang, C. Carlos, C. Zhang, K. Bhawnani, J. Li, J. Wang, P. M. Voyles, I. Szlufarska and X. Wang, *Chem. Mater.*, 2019, **31**, 9040–9048.
30 R. Makiura, K. Tsuchiyama, E. Pohl, K. Prassides, O. Sakata, H. Tajiri and O. Konovalov, *ACS Nano*, 2017, **11**, 10875–10882.
31 S. Li and H.-G. Liu, *Langmuir*, 2020, **36**, 10876–10884.
32 K. Yamanami, Y. Fujita, K. Matsui, R. Asari, T. Kusawake and T. K. Shimizu, *Langmuir*, 2022, **38**, 1910–1914.
33 M. K. Bera, T. Mori, T. Yoshida, K. Ariga and M. Higuchi, *ACS Appl. Mater. Interfaces*, 2019, **11**, 11893–11903.
34 I. Aratani, Y. Horii, Y. Kotani, H. Osawa, H. Tanida, T. Ina, T. Watanabe, Y. F. Yano, A. Mizoguchi, D. Takajo and T. Kajiwara, *J. Mater. Chem. C*, 2024, **12**, 724–735.
35 E. Biemmi, S. Christian, N. Stock and T. Bein, *Microporous Mesoporous Mater.*, 2009, **117**, 111–117.
36 J. Łuczak, M. Kroczewska, M. Baluk, J. Sowik, P. Mazierski and A. Zaleska-Medynska, *Adv. Colloid Interface Sci.*, 2023, **314**, 102864.
37 D. Ishikawa, T. Mori, Y. Yonamine, W. Nakanishi, D. L. Cheung, J. P. Hill and K. Ariga, *Angew. Chem., Int. Ed.*, 2015, **54**, 8988–8991.
38 I. Ciria-Ramos, I. Tejedor, L. Caparros, B. Doñagueda, O. Lacruz, A. Urtizberea, O. Roubeau, I. Gascón and M. Haro, *Dalton Trans.*, 2023, **52**, 7196–7207.
39 F. Bonosi, A. Renault and B. Berge, *Langmuir*, 1996, **12**, 784–787.
40 A. Dhanabalan, N. Prasanth Kumar, S. Major and S. S. Talwar, *Thin Solid Films*, 1998, **327–329**, 787–791.
41 G. B. Khomutov, A. M. Tishin, S. N. Polyakov and J. Bohr, *Colloids Surf., A*, 2000, **166**, 33–43.
42 K. Gong, S.-S. Feng, M. L. Go and P. H. Soew, *Colloids Surf., A*, 2002, **207**, 113–125.
43 K. Tachimoto, T. Ohata, K. J. Takeno, A. Nomoto, T. Watanabe, I. Hirosawa and R. Makiura, *Langmuir*, 2023, **39**, 8952–8962.
44 T. Ohata, K. Tachimoto, K. J. Takeno, A. Nomoto, T. Watanabe, I. Hirosawa and R. Makiura, *Bull. Chem. Soc. Jpn.*, 2023, **96**, 274–282.
45 K. Hoshiko, T. Kambe, R. Sakamoto, K. Takada and H. Nishihara, *Chem. Lett.*, 2014, **43**, 252–253.
46 T. Pal, T. Kambe, T. Kusamoto, M. L. Foo, R. Matsuoka, R. Sakamoto and H. Nishihara, *ChemPlusChem*, 2015, **80**, 1255–1258.
47 V. Rubio-Giménez, M. Galbiati, J. Castells-Gil, N. Almora-Barrios, J. Navarro-Sánchez, G. Escorcia-Ariza, M. Mattera, T. Arnold, J. Rawle, S. Tatay, E. Coronado and C. Martí-Gastaldo, *Adv. Mater.*, 2018, **30**, 1704291.
48 V. Rubio-Giménez, N. Almora-Barrios, G. Escorcia-Ariza, M. Galbiati, M. Sessolo, S. Tatay and C. Martí-Gastaldo, *Angew. Chem., Int. Ed.*, 2018, **57**, 15086–15090.

49 Z. Wang, L. S. Walter, M. Wang, P. St, B. Petkov, H. Liang, N. N. Qi, M. Nguyen, H. Hambsch, M. Zhong, S. Wang, L. Park, K. Renn, T. Watanabe, S. C. B. Taniguchi, T. Mannsfeld, U. Heine, S. Kaiser, R. T. Zhou, X. F. Weitz and R. Dong, *J. Am. Chem. Soc.*, 2021, **143**, 13624–13632.
50 D. Sheberla, L. Sun, M. A. Blood-Forsythe, S. Er, C. R. Wade, C. K. Brozek, A. Aspuru-Guzik and M. Dincă, *J. Am. Chem. Soc.*, 2014, **136**, 8859–8862.
51 R. W. Day, D. K. Bediako, M. Rezaee, L. R. Parent, G. Skorupskii, M. Q. Arguilla, C. H. Hendon, I. Stassen, N. C. Gianneschi, P. Kim and M. Dincă, *ACS Cent. Sci.*, 2019, **5**, 1959–1964.
52 M. E. Foster, K. Sohlberg, M. D. Allendorf and A. A. Talin, *J. Phys. Chem. Lett.*, 2018, **9**, 481–486.
53 T. Ohata, A. Nomoto, T. Watanabe, I. Hirosawa, T. Makita, J. Takeya and R. Makiura, *J. Colloid Interface Sci.*, 2023, **651**, 769–784.
54 P. Díaz, J. Benet-Buchholz, R. Vilar and A. J. P. White, *Inorg. Chem.*, 2006, **45**, 1617–1626.
55 H.-L. Jiang and Q. Xu, *CrystEngComm*, 2010, **12**, 3815–3819.
56 A. Schejn, L. Balan, V. Falk, L. Aranda, G. Medjahdi and R. Schneider, *CrystEngComm*, 2014, **16**, 4493–4500.
57 D. Bara, E. G. Meekel, I. Pakamorė, C. Wilson, S. Ling and R. S. Forgan, *Mater. Horiz.*, 2021, **8**, 3377–3386.
58 W. Zhao, T. Chen, W. Wang, B. Jin, J. Peng, S. Bi, M. Jiang, S. Liu, Q. Zhao and W. Huang, *Sci. Bull.*, 2020, **65**, 1803–1811.
59 Y. Qian, G. Xue, L. Chen, G. Xu and G. Wang, *Adv. Mater.*, 2024, **36**, 2310795.
60 F. Bigdeli, M. N. A. Fetzer, B. Nis, A. Morsali and C. Janiak, *J. Mater. Chem. A*, 2023, **11**, 22105–22131.